Energy Storage Materials 45 (2022) 412–421

Contents lists available at ScienceDirect

Energy Storage Materials

journal homepage: www.elsevier.com/locate/ensm

Fullerene-like elastic carbon coatings on silicon nanoparticles by solvent controlled association of natural polyaromatic molecules as high-performance lithium-ion battery anodes

Wen Tan[a,b], Fan Yang[c,*], Tingting Yi[b], Gang Liu[b], Xiaoting Wei[b], Qiurong Long[b], Yi Liu[b], Yingzhi Li[b], Chuanfei Guo[b], Kun Liu[b], Zhouguang Lu[b], Qingxia Liu[c], Zhenghe Xu[b,*]

[a] School of Materials Science and Engineering, Harbin Institute of Technology, Harbin 150001, China
[b] Department of Materials Science and Engineering, Shenzhen Key Laboratory of Interfacial Science and Engineering of Materials, Key University Laboratory of Highly Efficient Utilization of Solar Energy and Sustainable Development, Southern University of Science and Technology, Shenzhen 518055, China
[c] College of New Materials and New Energies, Shenzhen Technology University, Shenzhen 518055, China

A B S T R A C T

Carbon coating is one of the most common methods to improve the performance of Li-ion batteries, especially for materials such as silicon and silicon oxides (SiO_x) of poor electronic conductivity and large volume changes during cycling. However, its brittle nature and low elasticity make the conventional carbon coatings crack easily and hence lose the conductive connection with active materials after a few cycles. In this work, we propose a scalable and low-cost synthesis method to deposit a highly-elastic fullerene-like protective carbon layer on silicon nanoparticles by molecular-level controlled association of natural polyaromatic molecules in heavy oil. The fullerene-like carbon layer is shown to recover by > 90% after deformation, which ensures the structural stability of the carbon coatings during cycling. Fullerene-like carbon coated silicon nanoparticles exhibit a high cycle stability with a reversible capacity of 1230 mAh g^{-1} and capacity retention of 94.6% after 600 cycles at 1 C. These results demonstrate the great commercial potential of this synthesis method in producing anode materials of high-performance lithium-ion batteries.

1. Introduction

A considerable amount of research has been focused on high energy density LIBs to satisfy the desire for lighter and more durable electronics and electric vehicles [1,2]. Unfortunately, the high-capacity active materials, such as alloy-type materials [3], conversion-type materials [4,5], and sulfur cathodes [6], often suffer from poor electrical conductivity and huge volume changes during cycling [7,8]. For example, the commercial use of silicon anodes with a high energy density of 4200 mAh g^{-1} is prohibited by these inherent drawbacks which lead to poor rate properties, pulverization of active materials, continuous reconstruction of the solid-electrolyte interface (SEI) and rapid decay of battery capacity [9,10].

Nanostructures, such as nanowires [11], nanotubes [12], nanosheets [13], hollow/yolk-shell structures [14], porous Si [7,15] and others [16,17] have been proven to be potential solutions to some degree in mitigating the challenges from volume change by allowing extra freedom for the volume change of active silicon materials. Although improvements in electrochemical performance over pure silicon are often achieved by designing these complex silicon-carbon composites, the high cost, tedious manufacturing process and use of hazardous materials such as strong acids in manufacturing process limit the production of these materials only at lab-scales, diminishing if not prohibiting their commercial applications.

Carbon is commonly used as a protective layer on the outside of active materials or acts as an embedding matrix to improve electric conductivity and alleviate deleterious volume change [18–21]. Carbonization of organic precursors on the surface of silicon particles is the most straightforward synthesis method to form a carbonaceous outer shell on silicon, and therefore was one of the earliest attempts to deposit a protective carbon layer on silicon [22,23]. However, owing to its brittle nature, the conventional carbon coatings will easily crack after a few cycles, leaving silicon exposed to the electrolyte again to promot fast electrolyte consumption and excess growth of SEI. Low-elasticity carbon layer cannot fully recover after following the expansion of silicon during repeated electrochemical cycling, resulting in the loss of electrical contact between the silicon particles and the carbon coating [24]. Furthermore, carbon coatings with high Young's modulus will hinder the lithiation process by limiting the volume expansion of silicon [25]. It is hypothesized that an elastic carbon coating can offer a better mechanical stability to accommodate the volume change of the silicon during lithiation/delithiation cycles. Achieving elasticity in a carbon film requires fine adjustments of the ratio and linkage between tetrahedrally bonded carbons (sp^3-bonded) and π system-based (sp^2-bonded) carbons with fullerene-like structure [26]. For instance, anisotropic compression of fullerene-like carbons and carbon nanotubes against a substrate at a high velocity was a viable approach to offer high elasticity in the deposited carbon films [27]. Therefore, fullerene-like carbon is hypothesized to be an ideal protective structure for silicon-based anodes to

* Corresponding authors.
E-mail addresses: yangfan@sztu.edu.cn (F. Yang), xuzh@sustech.edu.cn (Z. Xu).

https://doi.org/10.1016/j.ensm.2021.11.040
Received 12 September 2021; Received in revised form 10 November 2021; Accepted 22 November 2021
Available online 14 December 2021

realize its superior micromechanical properties. However, techniques to form fullerene-like carbon spheres using for instance cathodic arc [26,28], laser ablation [29], or by heating nanodiamonds at extremely high temperatures [30] are usually costly and difficult for scale up production, not to mention the difficulties in controlling the mophology of carbon coatings.

In this work, we developed a new approach to prepare high elastic fullerene-like carbon films on silicon nanoparticles (Si NP) as the protection layer for high-performance lithium-ion batteries by using natural polyraomatic meolecules (asphaltenes, PAM) in heavy crude oil or petroleum refinery residues as the carbon source. An optimized aromaticity of solvents can promote the formation of desired PAM clusters on silicon nanoparticle surfaces, which can then be easily converted to an amorphous carbon coating with embedded fullerene-like carbon nanoscaffolds during a mild carbonization process. Silicon nanoparticles of fullerene-like carbon coatings synthesized in this study exhibited an excellent cycle stability and rate performance with an initial Columbic efficiency of 89.7%, and a remaining reversible capacity of 1230 mAh g^{-1} after 600 cycles at 1 C (1 C is 3579 mA g^{-1}) with capacity retention of 94.6%. The fullerene-like carbon coating can be further applied to improve the electrochemical performance of SiO microparticles. Due to strong adsorption and self-association of PAM on various surfaces, such a simple and efficient coating strategy is also applicable to the modification of other electrode materials. Owing to its high carbon content and versatile tunability, natural PAM as an abundant and low-cost by-product from petroleum industry has been widely used to prepare carbon-based materials for energy storage applications [31]. However, recent studies are mainly focused on the carbonization conditions and origin of the oil on the performance of carbonized products. Important findings from this molecular-level research on adsorption and self-assembly followed by carbonization of PAM open a new path of utilizing a cheap heavy oil or waste by-product of petroleum refineries as carbon source in production of carbon composite materials for energy storage applications.

2. Experimental section

2.1. Materials synthesis

Tol-SiNP and Hept-SiNP. Heavy oil (0.2 g) from Argentina was first dissolved in toluene (15 mL) (AR, Sinopharm) or heptol (a heptane to toluene volume ratio of 5:5). Then, silicon nanoparticles (0.6 g) of ~100 nm in size from Guangdong Canrd New Energy Technology Co. Ltd were dispersed in the heavy oil in toluene or heptol solutions. The suspension was stirred at room temperature for 12 h. After evaporation of the solvent in a rotary evaporator at 50 °C, the heavy oil-coated silicon nanoparticles were carbonized at 480 °C in Ar atmosphere for 1 h. The nanoparticles obtained as such were referred to as Tol-SiNP and Hept-SiNP, respectively, depending on the solvent used. For comparison, the same method was used to synthesize fullerene-like carbon coated SiO microparticles from heavy oil in heptol solvent.

Samples for Nanoindentation Measurements. Heavy oil (0.5 g) was dissolved in 50 mL toluene or heptol. A drop of the solution was then carefully placed on silicon wafers to allow solvent evaporation before being carbonized at 480 °C in Ar atmosphere for 1 h.

2.2. Materials characterization

Scanning electron microscopy (SEM, Tescan Vega 3 LMH), transmission electron microscopy (TEM) and high-angle annular dark field scanning transmission electron microscopy (HAADF-STEM) with energy dispersive X-ray spectrometry (EDS) (FEI Talos F200X) were used to characterize the morphology of the samples. TGA was performed using a Mettler instrument at a heating rate of 10 °C min^{-1} between 30 °C and 800 °C in N_2. Raman spectra were obtained using a Horiba JobinYvon. N_2 adsorption–desorption isotherms were obtained on a TriStar II 3020 system. The surface morphology and mechanical properties of the carbon-coated silicon wafers were determined using an AFM (Bruker, Dimension Icon) with a PeakForce QNM module.

2.3. Electrochemical characterizations

Silicon nanoparticles (or SiO microparticles) were mixed with carbon nanotubes (CNTs) and polyacrylamide (PAA) at a mass ratio of 8:1:1 and then dispersed in N-methylpyrrolidone (NMP) to obtain homogenous slurries. The slurries were spread on Cu foil substrate and dried at 100 °C for 12 h. The mass loading of Si in the working electrodes was about 0.7 g cm^{-2} (1 g cm^{-2} for SiO) for cycling performance and 0.35 g cm^{-2} for CV, EIS and GITT measurement (detiles in Supporting Information). The half-cells were assembled in a glove box using CR2016 coin cells with Li metal foil as the counter electrode. The electrolyte was 1 mol L^{-1} solution of $LiPF_6$ in a mixture of ethylene carbonate (EC), dimethyl carbonate (DMC) and diethyl carbonate (DEC) (1:1:1 by vol.) with 5 wt.% fluoroethylene carbonate (FEC). A polypropylene membrane was used as the separator. In a silicon full cell, the cathode contains super P/PVDF/NCM622 at a mass ratio of 10/10/80 on Al foil at a mass loading of 20 mg cm^{-2} NCM622, and the anode contains super P/PAA/silicon (10/10/80) on Cu foil at a mass loading of 1.6 mg cm^{-2} silicon. In a SiO full cell, the cathode contains super P/PVDF/$LiFePO_4$ at a mass ratio of 10/10/80 on Al foil at a mass loading of 11.5 mg cm^{-2} $LiFePO_4$, and the anode contains super P/PAA/SiO (10/10/80) on Cu foil at a mass loading of 1.5 mg cm^{-2} SiO. All electrochemical tests were carried out at room temperature. Galvanostatic charging/discharging tests were conducted on a Neware instrument (Shenzhen, China) over a potential range of 0.01–1.5 V (half-cell), 2.7–4.2 V (Si//NCM622 full-cell) and 2.5–3.5 V (SiO//$LiFePO_4$ full-cell). The specific capacitie calculations of the cells were based on the mass of Si/C composite. CV curves were collected between 0.01 V and 3.0 V. EIS characterization was conducted using a potentiostat (IVIUMnSTAT) in the frequency range of 1 MHz-0.1 Hz under an AC input of 5 mV amplitude. Each EIS spectrum was collected after 5 h relaxation period at different voltages.

3. Results and discussion

3.1. Formation mechanism of fullerene-like carbons

The concept of solvent-controlled surface adsorption and self-association of polyaromatic molecules (PAM) on silicon nanoparticles in heavy oil is illustrated in Fig. 1. Being the heaviest components of heavy oil, asphaltenes are a mixture of PAMs which are soluble in aromatic solvent such as toluene and insoluble in aliphatic solvent such as heptane [32]. The structure of the adsorbed asphaltene layers depends therefore heavily on aromaticity of the solvent [33]. Asphaltenes of polyaromatic nature are anticipated to adsorb and self-assemble on Si NP in organic solvents through π-π association of polyaromatic rings, forming a viscoelastic adsorption layer [34–36]. Asphaltene clusters as building blocks were formed to scaffold on the surface of silicon nanoparticles in a solvent through the control of solvent aromaticity by varying heptane to toluene volume ratio of solvents. As heptane is added gradually into the heavy oil-in-toluene solution, asphaltene molecules become increasingly aggregated and eventually form large precipitates in a heptane-dominated solvent. During this process, asphaltenes adsorb progressively on silicon nanoparticles covered by a thin oxide layer (Figure S1, Supporting Information) until the formation of desired asphaltene clusters in a solvent of optimal aromaticity at a heptane to toluene volume ratio of 5:5 (heptol). Different from the dense adsorption in toluene, asphaltene clusters formed in heptol solvent become cross-linked on silicon surfaces to construct a cauliflower-like structure with its pores being filled and supported by maltenes (the non-asphaltene components of the heavy oil). Carbonization of this layer of hydrocarbons removes a majority of the maltenes due to their less carbon-forming nature, leading to an elastic coating of fullerene-like carbon nanoscaffolds embedded in

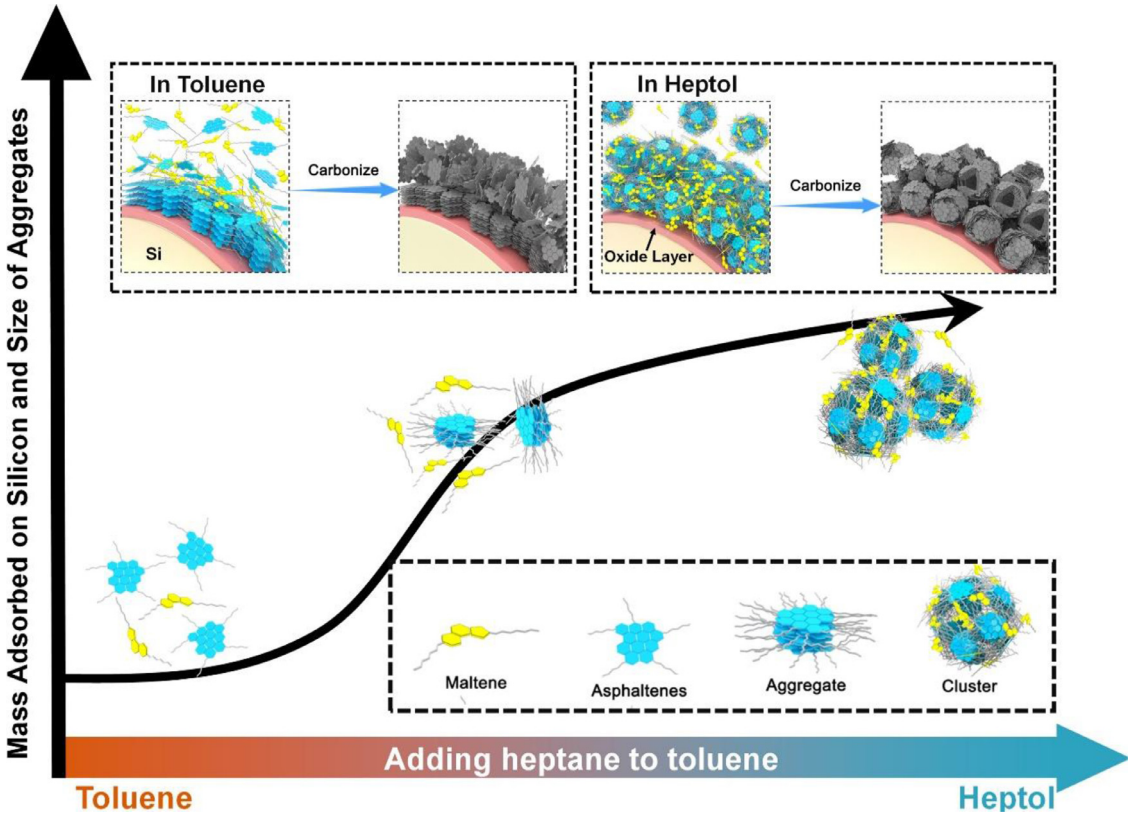

Fig. 1. Concept of the surface adsorption and self-association of PAM in heavy oil tuned at a molecular level by controlling the aromaticity of solvents to form fullerene-like structures of carbon coatings.

an amorphous carbon matrix. With pre-assembled structures of carbon precursors, the synthesis process for fullerene-like carbon is evidently much milder and easy to control than traditional methods.

3.2. Characterization of the fullerene-like carbon coated silicon

To demonstrate the controllability of asphaltene assembly by changing the aromaticity of solvent, heavy oil was first dissolved in toluene, followed by the addition of heptane to shift the solvent property from aromatic to more paraffinic, which triggers the formation of asphaltene clusters. The volume ratio of toluene to heptane in the final solvent was varied from 10:0 to 5:5 and 2:8. The morphology of heavy oil from different solvents and its carbonized products was examined by transmission electron microscopy (TEM). Fig. 2a shows a high dependence of the morphology of heavy oil precursors on the aromaticity of the solvent. Only when the aromaticity of the solvent is intermediate at a heptane to toluene volume ratio of 5:5, do the graphene-like layers of asphaltenes tangle with each other to form cauliflower-like structures. Formation of such a structure likely requires both the stacked asphaltene aggregates to provide “rigid” building blocks and flexible maltene molecules that can have a certain association with the stacked asphaltene aggregates to “fill up” the internal spaces among the aggregates (Figure S2). When solvency power is more aromatic (10:0) or highly paraffinic (2:8), such cauliflower-like structures cannot form due to the lack of desirable aggregates to stack in aromatic solvent environment or asphaltene-maltene phase segregation in paraffinic solvent environment (see Figure S3).

Carbonization of the heavy oil precursor with the cauliflower-like structure prepared in heptol produced a large amount of fullerene-like carbon spheres embedded in an amorphous carbon matrix. The fullerene-like carbon observed here was formed at a low carbonization temperature of 480 °C, indicating a significantly lower temperature of carbonization to preserve fullerene-like structures pre-assembled from PAMs in heptol. This mild synthesis process can significantly reduce the cost of synthesizing the fullerene-like carbons and be easily applied to carbon coatings of silicon nanoparticles. Silicon nanoparticles were dispersed in a heavy oil in heptol solution. After 24 h, the solvent was evaporated, forcing the remaining non-adsorbed organics (mostly maltenes) into the pores and onto the surface of asphaltene scaffolds assembled on the silicon nanoparticles. The nanoparticles were subsequently carbonized at 480 °C (Figure S4) to produce Hept-Carbon-coated silicon nanoparticles (Hept-SiNP). The same process was repeated using toluene as the solvent to prepare Tol-Carbon-coated silicon nanoparticles (Tol-SiNP) for comparison (Figure S5). The peak of carbon at 1360 cm^{-1} and 1580 cm^{-1} in the Raman spectrum proves the successful coatings of carbon on silicon (Figure S6).

Compared with the adsorbed layer of surface-active asphaltenes in toluene, the scaffolded layer formed on silicon nanoparticles in heptol features more homogenous structures and fullerene-like carbon regions (Fig. 2b). Such a feature allows more maltenes to be incorporated in the structure and leads to a thicker and homogeneous single-layer structure in the carbon coating of Hept-SiNP. Dual structure, on the other hand, was observed in the carbon layer on Tol-SiNP (Fig. 2e), which is caused by maltene-asphaltene segregation due to their significant differences in surface activity of adsorption on silicon surfaces in toluene. In thermogravimetric analysis (TGA), the Hept-SiNP were shown to lose a significantly more weight than Tol-SiNP during carbonization at 480 °C (Figure S7), which corresponds to a Si content of 92.3 wt.% and 89.2 wt.% for Hept-SiNP and Tol-SiNP, respectively (Figure S8). This finding results from a denser adsorbed layer of asphaltenes in the toluene, which is easier to carbonize in the subsequent thermal carbonization process.

To closely examine the structure of the carbon layers in Tol-SiNP and Hept-SiNP, the silicon substrates were removed using NaOH aqueous solutions while the carbon phases were recovered by centrifugation and analyzed by TEM (Fig. 2c and 2f). The recovered carbon appeared to be consisted of a continuous carbon matrix containing holes that were originally occupied by silicon nanoparticles (microstructures

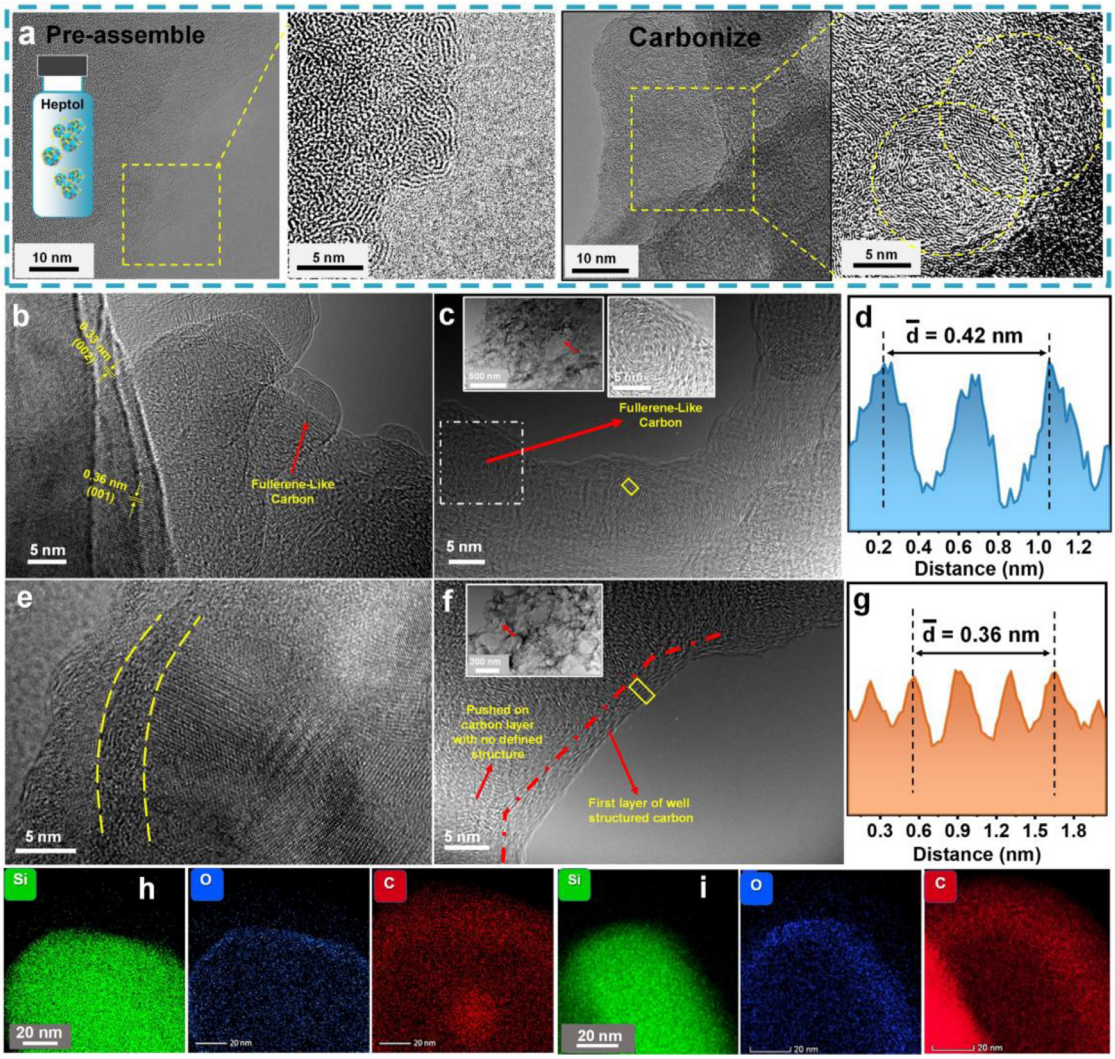

Fig. 2. Morphological characterization: **(a)** Structures resulting from asphaltene assembly in heptol before and after carbonization; **(b** and **e)** TEM micrographs of the carbonized layers on Hept-SiNP and Tol-SiNP, respectively; **(c** and **f)** TEM micrographs of the carbonized layers after removing silicon nanoparticles of Hept-SiNP and Tol-SiNP, respectively, with the insets showing the continuous carbon matrix; **(d** and **g)** D-spacing of the corresponding yellow regions in **c** and **f**, respectively; **(h** and **i)** EDS elemental mapping of Hept-SiNP and Tol-SiNP, respectively.

shown in the insets). Examination of the carbon layers on Hept-SiNP revealed fullerene-like carbon nanoscaffolds (in the order of 8 to 20 nm in size) concentrated in the region adjacent to the silicon surface (Fig. 2c). These carbon nanoscaffolds envelope a core that appears as a silicon nanoparticle being removed. It was well documented that the formation of fullerene-like structures usually creates internal stresses. These stresses arise from the curvature of the carbon planes and an already existing structure in which the graphitic sheets are restricted in lateral motion [37,38]. Such deformation stress is likely the main reason for the observed elasticity of the fullerene-based carbon coatings in Hept-SiNP.

The carbon coating on Tol-SiNP exhibits a structured inner layer at the edge of the hole and an amorphous carbon layer away from the hole. The inner structure consists of parallel carbon layers, suggesting the precursor asphaltene molecules being adsorbed on the silicon surface through stacking of polyaromatic rings (Fig. 2f). Heteroatoms such as O, N, and S in PAM are generally considered to be concentrated in ring systems [39]. The interaction of heteroatom-containing functional groups with the oxidized layer on silicon nanoparticles in toluene results in the adsorption of solvated asphaltene molecules in a flat-on configuration. The parallel graphitic orientation can only have in-plane covalent sp^2-bonds to support the volume expansion, while the weak interplanar van-der Waals bonds can easily result in 3-dimensional collapse of the carbon coating [40]. In addition to the differences in the morphologies of the carbon, the fullerene-like carbon in Hept-SiNP (Fig. 2d) features also a significantly greater D-spacing (4.2 Å) than the parallel carbon layers in Tol-SiNP (3.6 Å; Fig. 2g). The higher D-spacing in the film of Hept-SiNP likely results from the greater degree of freedom needed to form the fullerene geometry. Furthermore, the weak association and less ordered structure between asphaltene molecules in the heptol can contribute to the higher D-spacing observed in the final carbonized coating. The higher D-spacing may lead to a favourable binding of Li^+ ions and faster ion diffusion in the fullerene-like carbon.

Elemental mapping by energy dispersive X-ray spectroscopy (EDS) on Hept-SiNP (Fig. 2h) shows more scarcely and homogeneously distributed oxygen atoms in the single layer of carbon coatings. The Tol-SiNP (Fig. 2i) on the other hand features a first layer of enriched oxygen atoms. Such result corresponds well to the composition of asphaltenes which are enriched with oxygen containing functional groups. The second layer does not show any enrichment in oxygen atoms as anticipated, indicating the second layer being likely constructed by a mixture of maltenes and asphaltenes.

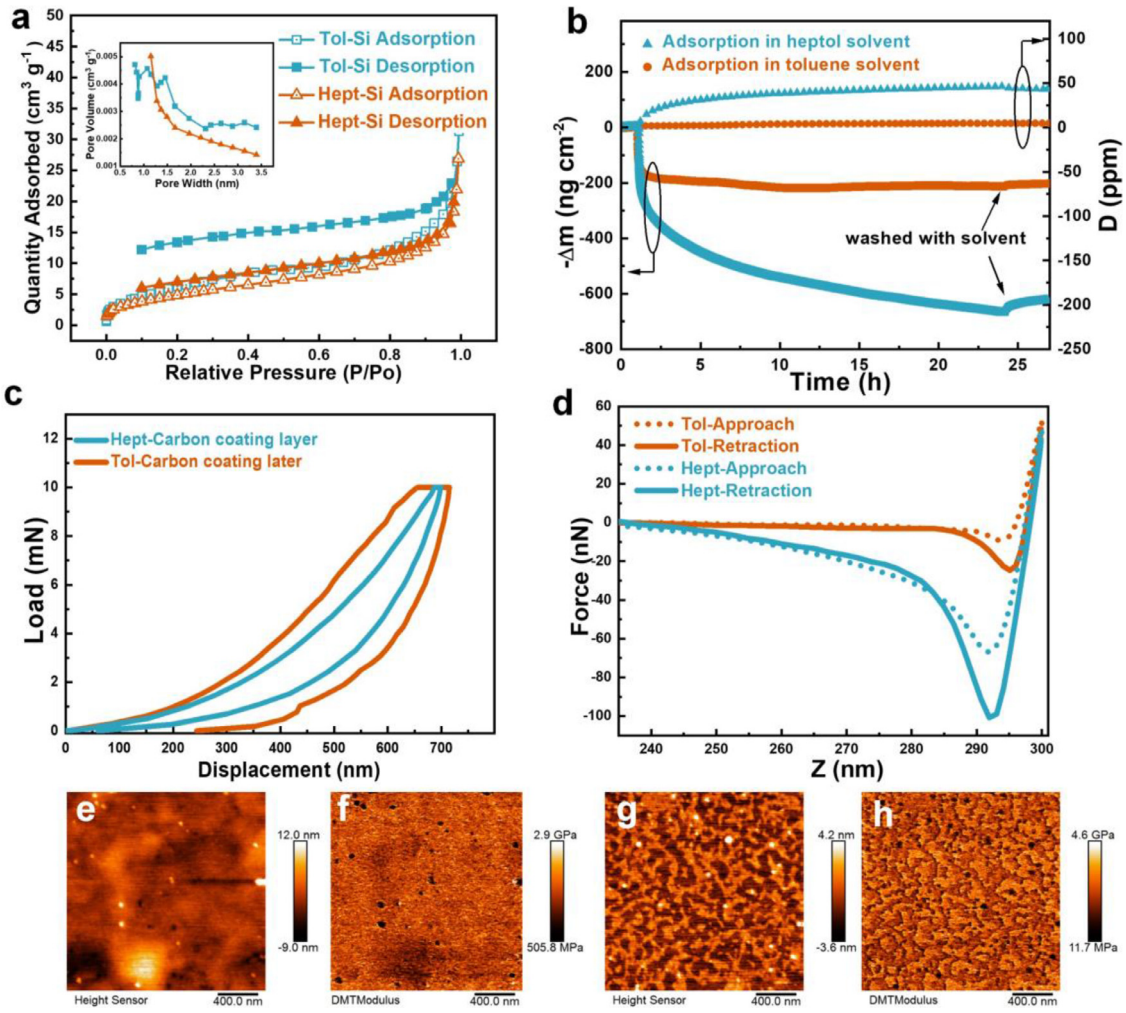

Fig. 3. Characteristics of carbon coatings: **(a)** Nitrogen adsorption and desorption isotherms for Tol-SiNP and Hept-SiNP, with the insets showing corresponding pore size distributions; **(b)** Adsorption isotherm of asphaltenes on silica sensor from different solvents determined in situ and in real time by a QCM-D instrument; **(c)** Nanoindentation trace of carbonized heavy oil coatings prepared using toluene and heptol on silicon wafer surfaces; **(d)** Force distance curves of carbon coatings; **(e** and **g)** Morphology of carbon coatings from toluene and heptol, respectively; **(f** and **h)** Nanomechanical map of carbon coatings from toluene and heptol, respectively.

More characterizations have further proven the unique structure and mechanical properties of this fullerene-like carbon coating. The porosity of Hept-SiNP was quantitatively determined by Brunauer-Emmett-Teller (BET) analysis using nitrogen as to be 0.048 $cm^3\ g^{-1}$which is 2.4 times higher than that of Tol-SiNP (0.020 $cm^3\ g^{-1}$) (Fig. 3a). Furthermore, a significant number of pores in Hept-SiNP are smaller than 1 nm, in contrast to the absence of pores in Tol-SiNP at this scale. These small pores in Hept-SiNP are anticipated to promote the diffusion of lithium ions.

The adsorption of heavy oil onto the silicon surface in toluene and heptol was quantitatively studied by quartz crystal microbalance with dissipation (QCM-D) measurements (Fig. 3b). A silica sensor was chosen here to represent the surface of silicon nanoparticles with a thin oxidation layer. The resonant frequency of the quartz oscillator (Δf) decreases with increasing the amount of heavy oil adsorbed [41]. The measured change in dissipation (D) indicates the change in the viscoelasticity and slip of adsorbed layers at the sensor-solution interface. A rigid layer of adsorption for instance, generates little change in dissipation, while a viscoelastic layer of adsorption in a good solvent causes a significant increase in dissipation [42]. Fig. 3b shows an adsorption plateau at 180 ng cm^{-2} onto the silica surface within 2 h in toluene, indicating a monolayer adsorption. Similar trends have been observed in the adsorption of heavy oil onto mica surfaces [43,44]. In the heptol, on the other hand, multilayer adsorption is observed, and the amount of asphaltenes adsorbed increased steadily with increasing adsorption time. The greater extent of molecular desorption upon washing with fresh solvent suggests the weak association between asphaltene aggregates in heptol solvent. The more significant increase in dissipation suggests a softer and more loosely-packed layer of heavy oil adsorbed on silica surfaces from heptol solutions than from toluene solutions, which builds the foundation for the elasticity of the carbon coating formed in heptol.

Nanoindentation trace (Fig. 3c) shows a substantially higher elasticity of the carbon coating layer on a silicon wafer derived from heptol (Hept-Carbon) than that from toluene (Tol-Carbon). When an incremental load from 1 to 10 mN was applied to the carbon layers, the deformation was found to be consistently greater for Hept-Carbon than Tol-Carbon. Maintaining a constant load of 10 mN on the coatings resulted in a further deformation of Tol-Carbon, likely caused by plane sliding or collapse of internal structures under the applied stress. For Hept-Carbon, on the other hand, deformation stopped almost immediately after stopping increase in the load. Upon removal of the load, deformation of the Hept-Carbon recovered almost completely (>90% recovery), suggesting a highly elastic nature of deformation. The fullerene-like nanostructure consisting of interlocked and curved graphite planes can extend a planar sp^2-coordinated carbon network into three dimensions, which can elastically store (absorb) the deformation energy by compression of the

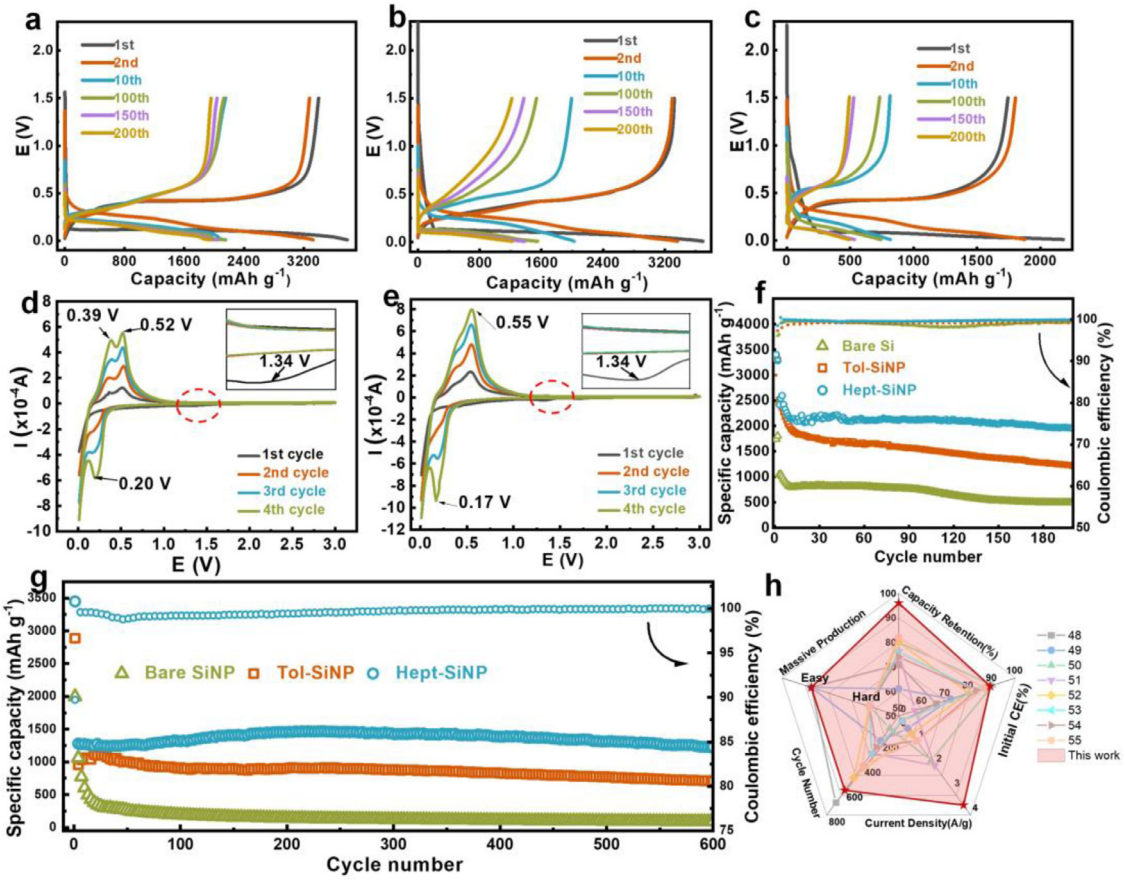

Fig. 4. Electrochemical performance of the synthesized Hept-SiNP in half-cell tests**:** Voltage profiles of Hept-SiNP **(a)**, Tol-SiNP **(b)** and Bare Si **(c)**; Cyclic voltammetry (CV) analysis of Hept-SiNP **(d)** and Tol-SiNP **(e); (f)** Cyclability at 0.2 C; **(g)** Long-term cyclability at 1 C; **(h)** Comparison of other carbon coated Si anodes. Refs. [48–55] are cited in this figure.

interplanar lattice spacing and carbon sheet buckling. Also shown in Fig. 3c is a much smaller hysteresis between loading and unloading cycles, indicating a less plastic (permanent) deformation and hence less fracture damage of Hept-Carbon film than Tol-Carbon film. This feature of deformation indicates a low elastic modulus and high fracture toughness in the Hept-Carbon film, which can act as an ideal coating on silicon to provide stable solid/electrolyte interface.

Fig. 3d shows the nano mechanical properties of carbon layers formed in the toluene and heptol systems, in the form of force-distance curves measured using Atomic Force Microscope (AFM). The z values at the valley points of the approaching curve (dotted curve) and retracting curve (solid curve) represent the displacement of the tip when the attachment or detachment occurred, respectively. The valley points of the approaching curve and retracting curve for the Hept-Carbon share the same Z values. This behavior demonstrates that the carbon layer on Hept-Carbon has recovered its shape when the tip was retracted and detached. For the Tol- Carbon system on the other hand, a significant hysteresis of around 1 nm was observed in the Z values, which is likely caused by the plastic deformation in the carbon layers.

The morphology and micromechanical properties of Hept-Carbon and Tol-Carbon coatings are shown in Fig. 3e-h. The Hept-Carbon on the silicon substrate showed a thicker and smoother morphology (Fig. 3e). The nanomechanical mapping showed a much softer carbonized layer of Hept-Carbon (Fig. 3f) than Tol-Carbon (Fig. 3h), with a maximum elastic modulus of only 2.9 GPa. On the other hand, Tol-Carbon showed a homogeneous bottom layer and a patchy top layer of domains. The bottom layer is likely formed by adsorption and assembly of the most surface active asphaltenes. These surface active asphaltenes are usually more polyaromatic with more heteroatoms such as O and S. These molecules tend to associate with each other through π-π interactions. Such π-π stacking can result in highly ordered structures in the carbonized layer, leading to higher elastic modulus observed in these regions as shown in Fig. 3h. The bright (high-height) domains in the carbonized layer are likely due to the adsorption of asphaltene nanoaggregates formed although limited in good solvent (Figure S9). This uneven structure will make Tol-Carbon easier to crack when silicon expands.

In summary, the fullerene-like carbon coating on silicon surface exhbits an elastic and soft nature, which ensures that the coating structure of carbon would not be destroyed during the continuous lithiation/delithiation processes of silicon. The higher porosity and D-space of Hept-Carbon can promote the diffusion of lithium ions and further realize the stable operation of Hept-SiNP at high rate. Due to the excellent mechanical properties and microstructure of the fullerene-like carbon layer, Hept-SiNP is believed to have superior electrochemical properties.

3.3. Electrochemical performance of Hept-SiNP

The electrochemical performance of the silicon nanoparticles with elastic fullerene-like carbon-coatings in lithium ion batteries was examined in both half-cell and full-cell configurations. Fig. 4a-c show the voltage profiles of various electrodes at the rate of 0.03 C for the first two cycles and 0.2 C for the subsequent cycles. The electrode of Hept-SiNP, which is carbonized at the optimized temperature of 480 °C (see Figures S10 and S11), has a high initial capacity of 3790 mAh g^{-1} and a good reversible delithiation capacity of 3400 mAh g^{-1}, corresponding to an initial Coulombic efficiency (ICE) of ca. 89.7%. The formation of SEI layers on silicon during the first cycle due to undesired reactions

between silicon and electrolyte in general decreases drastically the reversible capacity, resulting in a low ICE as seen for bare Si (ca. 79.9%). The increased ICE in the case of Hept-SiNP electrode indicates that the clusters of carbons coated on silicon nanoparticles decreased effectively the silicon/electrolyte interface to decrease the formation of SEI layers. For a bare Si electrode, the intrinsic conductivity of Si is low, which increases the impedance of the electrode during lithiation, resulting in large polarization. The deliverable capacity is thus reduced by this polarization effect. The similar effect was reported in literature [45–47]. From the 10th to 200th cycle, the capacities of Tol-SiNP and bare Si decreased significantly and the potential plateau of Tol-SiNP became more oblique, which may be due to the collapse of the active material structure and the increase of impedance. To understand the mechanism behind the improved electrochemical properties of the anodes, cyclic voltammetry (CV) analysis at a sweep rate 0.1 mV s^{-1} were conducted. For both Hept-SiNP (Fig. 4d) and Tol-SiNP (Fig. 4e), a small reduction peak appeared in the initial cathodic scan at around 1.34 V, corresponding to the formation of SEI layers. Such a reduction peak disappeared in the following cycles, suggesting that for both samples, SEI layers were mainly formed and stabilized in the first cycle and further SEI growth was discouraged in the following cycles. Anodic peaks ($E_{P,a}$) at 0.17 V for Tol-SiNP and 0.2 V for Hept-SiNP were attributed to the reduction of Si to LixSi alloy phases and the cathodic peaks ($E_{P,c}$) at 0.55 V for Tol-SiNP and 0.39 V, 0.52 V for Hept-SiNP were related to the phase transformation process from LixSi alloy to amorphous Si. The voltage gap between the anodic and cathodic peaks (peak potential separation, ΔE_P) indicates the amount of driving force needed for the Li^+ to move in or out of the anode materials and the rate of electrochemical reaction. Thus, a smaller ΔE_P of Hept-SiNP around 0.32 V with that of Tol-SiNP around 0.38 V suggests higher ionic conductivity and electrochemical activity of Hept-SiNP.

Fig. 4f shows that electrode with Hept-SiNP can run stably for 200 cycles at 0.2 C, showing a high reversible capacity of 1961 mAh g^{-1} and capacity retention of 95.1%. In contrast, the capacities of Tol-SiNP and bare SiNP decreased to 1217 and 896 mAh g^{-1}, respectively after 200 cycles, even though their capacities were similar to Hept-SiNP in the first few cycles. The enhanced cycle stability of Hept-SiNP is mainly attributed to the excellent mechanical properties of the fullerene-like carbon coating on silicon nanoparticles, which can provide a stable solide/electrolyte interface during the lithiation/de-lithiation process. The Hept-SiNP electrode exhibits higher specific capacities at various current density as compared with Tol-SiNP and bare SiNP electrodes (Figure S12). Even at a high rate of 1 C, Hept-SiNP still showed a remarkable long-term cycle stability (Fig. 4g). After 600 cycles, Hept-SiNP retained a high reversible capacity of 1230 mAh g^{-1}, correponding to capacity retention of 94.3% based on the capacity of the fourth cycle. While, the capacity of Tol-SiNP has continued to decrease to 707 mAh g^{-1}. The micropores in the fullerene-like carbon coating can improve the kinetics of lithium ion transmission and impart Hept-SiNP excellent rate performance. Compared with previous studies on carbon-coated silicon nanoparticles (Fig. 4h), Hept-SiNP prepared using our approach has clearly improved electrochemical properties and showed a comparable electrochemical performance with other existing Si/C composites of complex structures which are difficult if not impossible to commercialize.[48–55]

In situ electrochemical impedance spectroscopy (EIS) analyses were conducted at various pre-chosen potentials during the initial and 20th lithiation processes (Fig. 5a). Starting from an open circuit potential of 2.6 V, the 1st and 20th charge-discharge cycles were conducted between 0.01–3.0 V and 0.01–1.6 V, respectively at a current density of 0.1 A g^{-1}. A full-featured in situ Nyquist plot includes a semicircle in each of the high and medium-frequency regions and a sloped line in the low-frequency region, which are dependent on the interfacial resistances due to SEI passivation (R_{sei}), the contact resistance/charge transfer resistance (R_{ct}) and the diffusion kinetics of Li^+ in the bulk phase of the active materials, respectively. A corresponding equivalent circuit is then obtained with IviumSoft, which includes two sections, R_{sei} and R_{ct}, that account for the charge-transfer resistance of the SEI layer and the carbon coating on the active materials, respectively. The sum of R_{sei} and R_{ct} (R_{tot}) is shown in Fig. 5b. In the first lithiation scan, R_{tot} for both Tol-SiNP and Hept-SiNP started to increase after 1.5 V, suggesting the decrease in overall conductivity due to the volumetric expansion/phase transformation of the silicon during lithiation. Evidently, R_{tot} values of Hept-SiNP is lower than Tol-SiNP at each pre-chosen voltage, likely due to the preferable improvement of the interfacial kinetics of Li^+ in Hept-SINP. After the 20 charge/discharge cycles, R_{tot} value of Tol-SINP at 1.5 V (before lithiation) has significantly increased. The phenomenon is commonly observed in silicon-based anodes due to the loss of conductive connection between silicon and the carbon matrix by the repeated volume change of the active material and continuous growth of SEI layers. With the decrease in the voltage of Tol-SiNP, the value of R_{tot} decreased significantly, as a result of destroying the existing SEI layer and exposing fresh Si to the electrolyte by the expanded silicon. It is interesting to note that the R_{tot} values of Hept-SINP at the 20th cycle decreased as compared with the first cycle. The improvement is likely due to irreversible volume expansion which makes the contact between the active material, conductive additive and the current collector stronger. Due to the high elasticity of the fullerene-like carbon coating, the carbon coating can keep its structure after being forced to expand by silicon, and always keeps in conductive contact with silicon. The galvanostatic intermittent titration technique (GITT) was used to obtain the diffusion coefficient of lithium (D_{Li}) at various stoichiometric compositions of Li_xSi. As shown in Fig. 5c, the Li^+ diffusion coefficient was consistently higher in Hept-SiNP than in Tol-SiNP as anticipated. The same trend was observed in cyclic voltammetry (CV) (Figure S13).

The structures of the active materials of electrodes after 100 cycles were characterized through TEM imaging and element mapping using energy dispersive X-ray spectroscopy (EDS). For Hept-SiNP, the structure of the active material is essentially intact (Fig. 5d), and the F element (representative of SEI growth) was found to be concentrated only outside of the composites and the shape of the silicon nanoparticles remained well defined (Fig. 5e). As shown in the high-resolution TEM micrograph (Figure S14), the carbon coatings in Hept-SiNP after 100 cycles retained its fullerene-like structure. The effective separation between the SEI layer and the silicon NPs can still be clearly observed. In contrast, the carbon coating in Tol-SiNP showed a sponge-like structure (as shown in Fig. 5f) and a thick and homogenous SEI (Fig. 5g) due to the disruption of its carbon coatings. Similar structure was proposed in a recent report to explain the capacity fading of silicon anode, caused by progressive growth of the solid-electrolyte interphase towards the interior of Si anode [56]. In-depth X-ray photoelectric spectroscopy (XPS) analysis was performed to identify surface chemistry of Hept-SiNP and Tol-SiNP after 100 cycles (Figure S15). Before sputtering, the Hept-SiNP and Tol-SiNP electrodes exhibit typical decomposition products of the organic solvent molecules. Li_4SiO_4 was measured only on Tol-SiNP, indicating that the carbon protective layer on Tol-SiNP was disintegrated, which led to direct contact between Si and electrolyte. With the sputtering of Hept-SiNP from 50 s to 600 s, the intensity of LiF (inorganic component of SEI) bands decreased gradually, accompanied by an increase in the intensity of Si and Li_xSi. This finding indicates the presence of a thin SEI layer and effective separation of Si and SEI by robust Hept-carbon coatings. On the contrary, the high intensity of LiF at various sputtering time and the evident signal of Li_4SiO_4 for Tol-SiNP indicate the destruction of carbon coatings, a significant growth of SEI layer and direct contact between Si and electrolyte. These observations indicate the breaking of carbon layer originally formed on silicon and excess SEI growth through the cracks on the silicon surface (Fig. 5h). After delithiation, the deformed carbon cannot be completely recovered, resulting in the loss of the connection between the active material and the carbon matrix. The clear difference between Hept-SiNP and Tol-SiNP after 100 cycles provides a clear indication that the integrity of the carbon

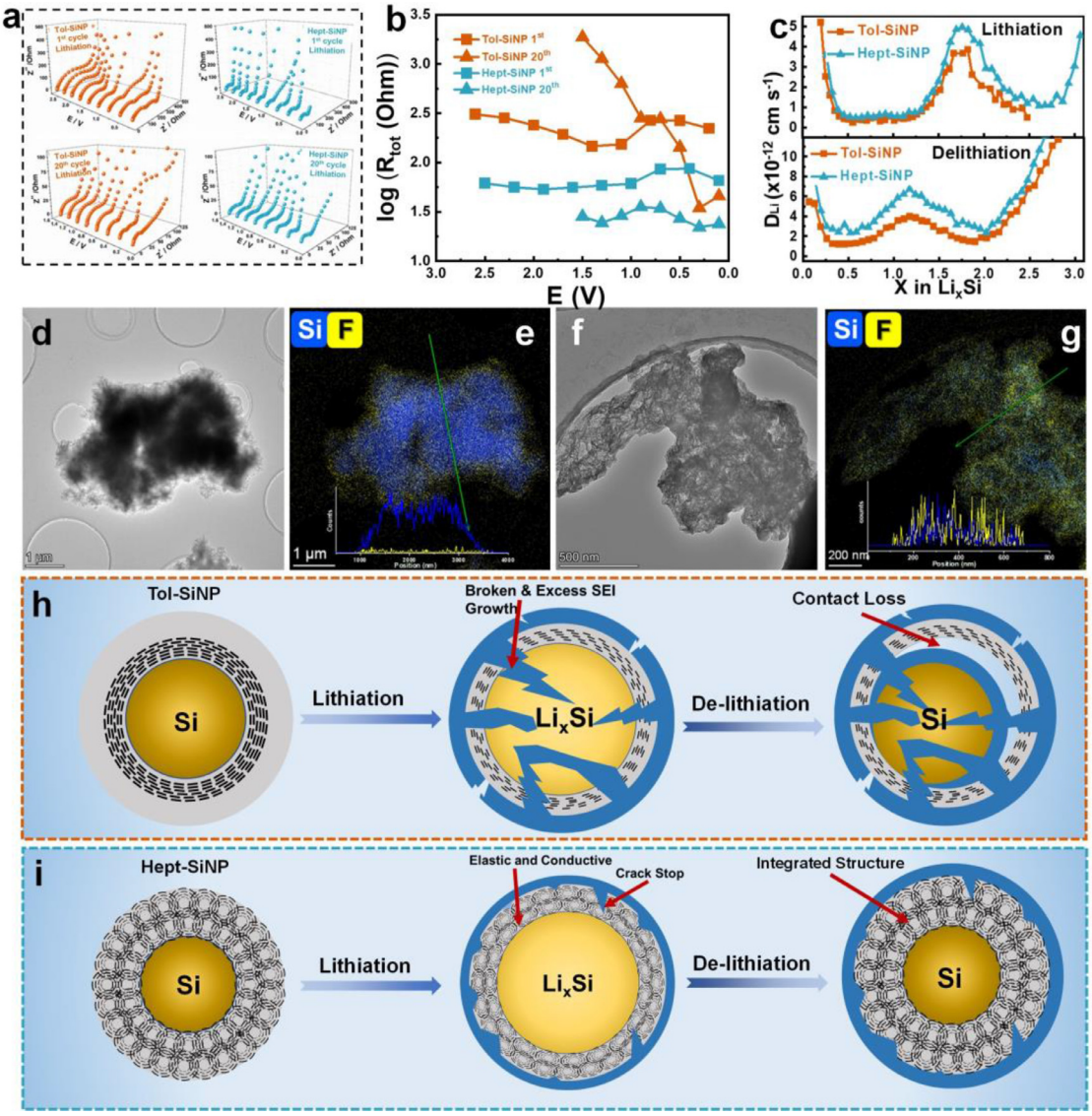

Fig. 5. Mechanism of improving the electrochemical performance of Si. (a) In-situ EIS of Tol-SiNP and Hept-SiNP at the 1st and 20th cycle; **(b)** R_{tot} calculated from the in situ EIS results; **(c)** Li^+ diffusion coefficient from GITT tests; **(d** and **f)** TEM images for Hept-SiNP and Tol-SiNP after 100 cycles, respectively; **(e** and **g)** EDS element mapping for Hept-SiNP and Tol-SiNP after 100 cycles, respectively; **(h** and **i)** Schematics of SEI growth in Tol-SiNP and Hept-SiNP, respectively.

layer remained during lithiation/delithiation in Hept-SiNP due to the improved robustness and elasticity (Fig. 5i).

To demonstrate the scalability of this synthesis scheme for commercial production, about 65 g of Hept-SiNP were synthesized in laboratory (Figure S16) and the heptol solvent was recovered through rotary evaporator. The massive produced Hept-SiNP was tested in a pouch cell with $LiNi_{0.6}Co_{0.2}Mn_{0.2}O_2$ (NCM622) as the cathode (Figure S17) at a n/p ratio of 1.2 based on the initial capacities. After three activation cycles at 0.01 C (Figure S18), the NCM622//Hept-SiNP full cell exhibted a high areal capacity of 2.8 mAh cm^{-2} and Coulombic efficiency of 97.2% at 0.2 C (Fig. 6a). In the following cycles, the coulombic efficiency quickly reached over 99%. After 100 cycles, the full-cell remained a high areal capacity of 2.4 mAh cm^{-2} with a capacity retention of 85.7% (Fig. 6b), confirming an effective and stable function of Hept-SiNP in a commercial cell. This synthesis method of fullerene-like carbon coatings can also be used to improve the electrochemical performance of SiO microparticles (Fig. 6c). The carbon coated SiO microparticles (SiO@C) (Fig. 6d) showed a reversible capacity of 1406 mAh g^{-1} after 250 cycles at 0.5 A g^{-1} with a capacity retention of 92.6% in half cell (Fig. 6e) and a capacity of 970 mAh g^{-1} after 300 cycles at 0.5 A g^{-1} with a capacity retention of 77.5% in full cell coupled with $LiFePO_4$ (Fig. 6f,g). The results demonstrate that the elastic fullerene-like carbon coatings on silicon nanoparticles and SiO microparticles prepared via the interfacial scaffolding of asphaltene aggregates can effectively improve the electrochemical reaction kinetics and electrode stability of silicon-based anodes. The massive production of Hept-SiNP and the successful operation of Hept-SiNP in the pouch cell have revealed the application prospects of this new approach to prepare high elastic fullerene-like carbon coatings on Li-ion battery materials.

4. Conclusion

A high elastic fullerene-like carbon coating was prepared by adjusting the adsorption and self-assembly of PAM in heavy oil on silicon nanoparticles. This synthesis method has highly reduced the difficulty of producing fullerene-like carbon. In addition, molecular-level controlled association of heavy oil offers new opportunities in utilizing heavy oil,

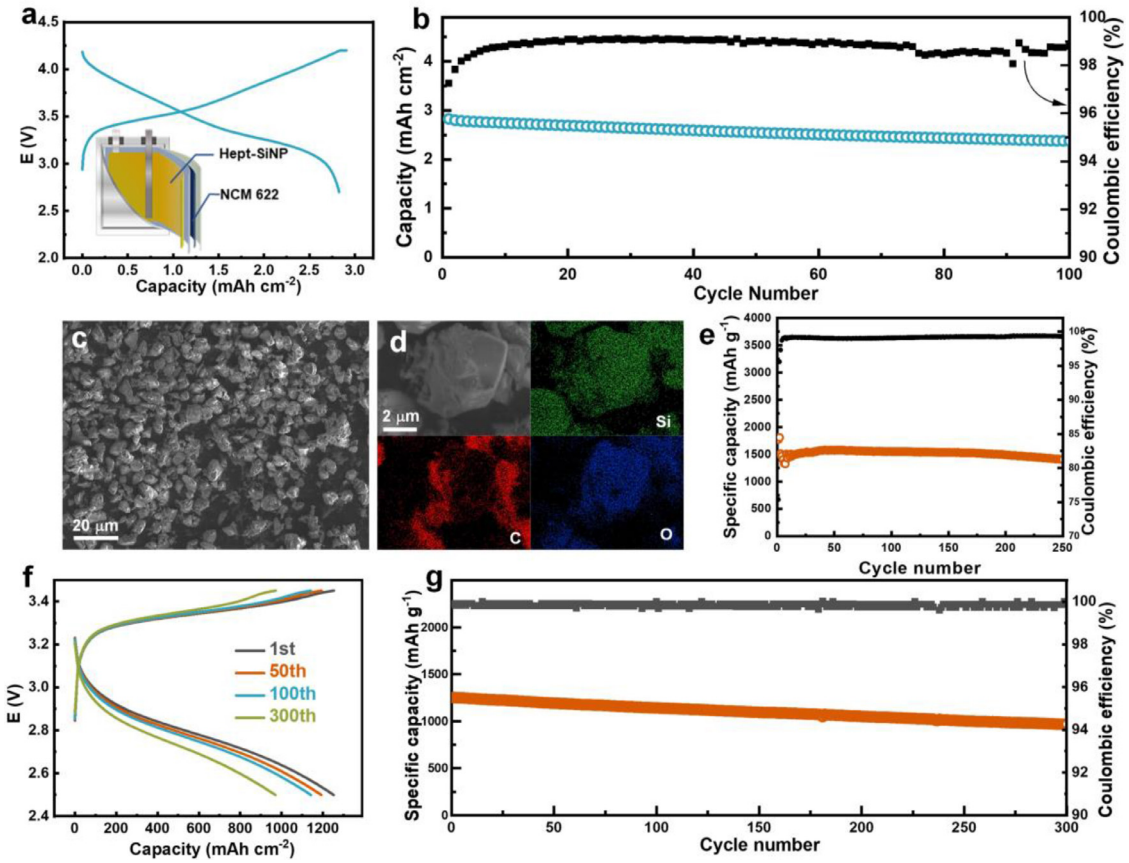

Fig. 6. Practical application of the fullerene-like carbon coatings: (a) Voltage profiles for the first cycle of the full cell at 0.2 C using Hept-SiNP as the anode and NCM622 as the cathode; **(b)** Full cell cyclability of Hept-SiNP at 0.2 C; **(c)** SEM image of SiO@C; **(d)** magnified SEM image and elemental mapping of SiO@C; **(e)** Half-cell cyclability of SiO@C; **(f)** Voltage profiles of the full cell using SiO@C as the anode and $LiFePO_4$ as the cathode; **(g)** Full-cell cyclability of SiO@C.

which has been widely used to prepare carbon-based materials for energy storage applications. The performance of carbon-coated silicon anodes is enhanced drastically by the ability of the coating to accommodate volume changes of silicon during lithiation/delithiation process, while allowing fast diffusion kinetics to facilitate Li^+ transfer. Due to the strong adsorption and self-association of polyaromatic molecules in heavy oil on various surfaces, such a simple and efficient coating strategy is applicable to modifications of other electrode materials. The fabrication method demonstrated in this study is facile and scalable for commercial production to meet the rapid growing need of the EV industry.

CRediT authorship contribution statement

Wen Tan: Conceptualization, Methodology, Software, Data curation, Investigation, Writing - original draft. **Fan Yang:** Conceptualization, Methodology, Project administration, Funding acquisition. **Tingting Yi:** Validation, Resources. **Gang Liu:** Investigation. **Xiaoting Wei:** Investigation. **Qiurong Long:** Investigation. **Yi Liu:** Resources. **Yingzhi Li:** Writing - Review & Editing. **Chuanfei Guo:** Writing - Review & Editing. **Kun Liu:** Investigation. **Zhouguang Lu:** Writing - Review & Editing, Project administration, Funding acquisition. **Qingxia Liu:** Writing - Review & Editing. **Zhenghe Xu:** Conceptualization, Writing - Review & Editing, Supervision, Project administration, Funding acquisition. These authors contributed equally: Wen Tan, Fan Yang.

Declaration of Competing Interest

There are no conflicts to declare.

Acknowledgements

The work was supported by the National Natural Science Foundation of China (Grant No. 21808101), Leading Talents of Guangdong Province Program (Grant No. 2016LJ06C536), Shenzhen Key Laboratory of Interfacial Science and Engineering of Materials (Grant No. ZDSYS20200421111401738), Research Foundation for Advanced Talents (Grant No. 20200207), and Guangdong-Hong Kong-Macao Joint Laboratory (Grant No. 2019B121205001). The authors also thank the Analytical and Testing Center of SUSTech for the measurements.

Supplementary materials

Supplementary material associated with this article can be found, in the online version, at doi:10.1016/j.ensm.2021.11.040.

References

[1] Y. Cao, M. Li, J. Lu, J. Liu, K. Amine, Bridging the academic and industrial metrics for next-generation practical batteries, Nat. Nanotechnol. 14 (2019) 200–207, doi:10.1038/s41565-019-0371-8.
[2] Y.Y. Liu, Y.Y. Zhu, Y. Cui, Challenges and opportunities towards fast-charging battery materials, Nat. Energy 4 (2019) 540–550, doi:10.1038/s41560-019-0405-3.
[3] K.H. Seng, M.-.H. Park, Z.P. Guo, H.K. Liu, J. Cho, Self-assembled germanium/carbon nanostructures as high-power anode material for the lithium-ion battery, Angew. Chem. Int. Ed. 51 (2012) 5657–5661, doi:10.1002/anie.201201488.
[4] P. Poizot, S. Laruelle, S. Grugeon, L. Dupont, J. Tarascon, Nano-sized transition-metal oxides as negative-electrode materials for lithium-ion batteries, Nature 407 (2000) 496–499, doi:10.1038/35035045.
[5] D.-.S. Liu, D.-.H. Liu, B.-.H. Hou, Y.-.Y. Wang, J.-.Z. Guo, Q.-.L. Ning, X.-.L. Wu, 1D porous MnO@N-doped carbon nanotubes with improved Li-storage properties as advanced anode material for lithium-ion batteries, Electrochim. Acta 264 (2018) 292–300, doi:10.1016/j.electacta.2018.01.129.

[6] N. Jayaprakash, J. Shen, S.S. Moganty, A. Corona, L.A. Archer, Porous hollow carbon@sulfur composites for high-power lithium-sulfur batteries, Angew. Chem. Int. Ed. 50 (2011) 5904–5908, doi:10.1002/anie.201100637.
[7] Y.L. An, Y. Tian, H. Wei, B.J. Xi, S.L. Xiong, J.K. Feng, Y.T. Qian, Porosity- and graphitization-controlled fabrication of nanoporous silicon@carbon for lithium storage and its conjugation with mxene for lithium-metal anode, Adv. Funct. Mater. (2019) 30, doi:10.1002/adfm.201908721.
[8] K. Feng, M. Li, W. Liu, A.G. Kashkooli, X. Xiao, M. Cai, Z. Chen, Silicon-Based Anodes for Lithium-Ion Batteries: from Fundamentals to Practical Applications, Small 14 (2018), doi:10.1002/smll.201702737.
[9] N. Liu, Z. Lu, J. Zhao, M.T. McDowell, H.W. Lee, W. Zhao, Y. Cui, A pomegranate-inspired nanoscale design for large-volume-change lithium battery anodes, Nat. Nanotechnol. 9 (2014) 187–192, doi:10.1038/nnano.2014.6.
[10] J. Sung, J. Ma, S.H. Choi, J. Hong, N. Kim, S. Chae, Y. Son, S.Y. Kim, J. Cho, Fabrication of lamellar nanosphere structure for effective stress-management in large-volume-variation anodes of high-energy lithium-ion batteries, Adv. Mater. 31 (2019) e1900970, doi:10.1002/adma.201900970.
[11] C.K. Chan, R.N. Patel, M.J. O'Connell, B.A. Korgel, Y. Cui, Solution-grown silicon nanowires for lithium-ion battery anodes, ACS Nano 4 (2010) 1443–1450, doi:10.1021/nn901409q.
[12] H. Wu, G. Chan, J.W. Choi, I. Ryu, Y. Yao, M.T. McDowell, S.W. Lee, A. Jackson, Y. Yang, L.B. Hu, Y. Cui, Stable cycling of double-walled silicon nanotube battery anodes through solid-electrolyte interphase control, Nat. Nanotechnol. 7 (2012) 309–314, doi:10.1038/Nnano.2012.35.
[13] W.S. Kim, Y. Hwa, J.H. Shin, M. Yang, H.J. Sohn, S.H. Hong, Scalable synthesis of silicon nanosheets from sand as an anode for Li-ion batteries, Nanoscale 6 (2014) 4297–4302, doi:10.1039/c3nr05354g.
[14] L. Zhang, C. Wang, Y. Dou, N. Cheng, D. Cui, Y. Du, P. Liu, M. Al-Mamun, S. Zhang, H. Zhao, A yolk-shell structured silicon anode with superior conductivity and high tap density for full lithium-ion batteries, Angew. Chem. Int. Ed. 58 (2019) 8824–8828, doi:10.1002/anie.201903709.
[15] M.Y. Ge, J.P. Rong, X. Fang, A.Y. Zhang, Y.H. Lu, C.W. Zhou, Scalable preparation of porous silicon nanoparticles and their application for lithium-ion battery anodes, Nano Res 6 (2013) 174–181, doi:10.1007/s12274-013-0293-y.
[16] D.C. Lin, Z.D. Lu, P.C. Hsu, H.R. Lee, N. Liu, J. Zhao, H.T. Wang, C. Liu, Y. Cui, A high tap density secondary silicon particle anode fabricated by scalable mechanical pressing for lithium-ion batteries, Energy Environ. Sci. 8 (2015) 2371–2376, doi:10.1039/c5ee01363a.
[17] Y.Z. Jiang, Y. Li, P. Zhou, Z.Y. Lan, Y.H. Lu, C.Z. Wu, M. Yan, Ultrafast, highly reversible, and cycle-stable lithium storage boosted by pseudocapacitance in Sn-based alloying anodes, Adv. Mater. (2017) 29, doi:10.1002/adma.201606499.
[18] J. Wu, Y. Cao, H. Zhao, J. Mao, Z. Guo, The critical role of carbon in marrying silicon and graphite anodes for high-energy lithium-ion batteries, Carbon Energy 1 (2019) 57–76, doi:10.1002/cey2.2.
[19] Y. Liu, Z. Tai, T. Zhou, V. Sencadas, J. Zhang, L. Zhang, K. Konstantinov, Z. Guo, H.K. Liu, An All-Integrated Anode via Interlinked Chemical Bonding between Double-Shelled-Yolk-Structured Silicon and Binder for Lithium-Ion Batteries, Adv. Mater. (2017) 29, doi:10.1002/adma.201703028.
[20] H. Huang, X. Luo, Y. Yao, X. Zhou, Y. Jiang, C. Guo, J. Liu, X. Wu, Y. Yu, Binding Se into nitrogen-doped porous carbon nanosheets for high-performance potassium storage, Infomat 3 (2021) 421–431, doi:10.1002/inf2.12176.
[21] M. Yang, Q. Ning, C. Fan, X. Wu, Large-scale Ni-MOF derived Ni3S2 nanocrystals embedded in N-doped porous carbon nanoparticles for high-rate Na+ storage, Chin. Chem. Lett. 32 (2021) 895–899, doi:10.1016/j.cclet.2020.07.014.
[22] X.H. Shen, Z.Y. Tian, R.J. Fan, L. Shao, D.P. Zhang, G.L. Cao, L. Kou, Y.Z. Bai, Research progress on silicon/carbon composite anode materials for lithium-ion battery, J. Energy Chem. 27 (2018) 1067–1090, doi:10.1016/j.jechem.2017.12.012.
[23] X. Li, M. Zhang, S. Yuan, C. Lu, Research progress of silicon/carbon anode materials for lithium-ion batteries: structure design and synthesis method, Chemelectrochem 7 (2020) 4289–4302. doi:10.1002/celc.202001060.
[24] Q. Shi, J. Zhou, S. Ullah, X. Yang, K. Tokarska, B. Trzebicka, H.Q. Ta, M.H. Ruemmeli, A review of recent developments in Si/C composite materials for Li-ion batteries, Energy Storage Materials 34 (2021) 735–754, doi:10.1016/j.ensm.2020.10.026.
[25] J. Ryu, T. Bok, S.H. Joo, S. Yoo, G. Song, S.H. Kim, S. Choi, H.Y. Jeong, M.G. Kim, S.J. Kang, C. Wang, S.K. Kwak, S. Park, Electrochemical scissoring of disordered silicon-carbon composites for high-performance lithium storage, Energy Storage Materials 36 (2021) 139–146, doi:10.1016/j.ensm.2020.12.023.
[26] I. Alexandrou, H.-J. Scheibe, C. Kiely, A. Papworth, G. Amaratunga, B. Schultrich, Carbon films with an sp^2 network structure, Physical Review B 60 (1999) 10903, doi:10.1103/PhysRevB.60.10903.
[27] G.A.J. Amaratunga, M. Chhowalla, C.J. Kiely, I. Alexandrou, R. Aharonov, R.M. Devenish, Hard elastic carbon thin films from linking of carbon nanoparticles, Nature 383 (1996) 321–323, doi:10.1038/383321a0.
[28] M.D. Tucker, Z. Czigány, E. Broitman, L.-.Å. Näslund, L. Hultman, J. Rosen, Filtered pulsed cathodic arc deposition of fullerene-like carbon and carbon nitride films, J. Appl. Phys. 115 (2014) 144312, doi:10.1063/1.4871179.
[29] S. Yang, H. Zeng, H. Zhao, H. Zhang, W. Cai, Luminescent hollow carbon shells and fullerene-like carbon spheres produced by laser ablation with toluene, J. Mater. Chem. 21 (2011) 4432–4436, doi:10.1039/c0jm03475d.
[30] V. Kuznetsov, Y.V. Butenko, Nanodiamond graphitization and properties of onion–like carbon, Synthesis, properties and applications of ultrananocrystalline diamond, Springer (2005) 199–216.
[31] H. Hu, M. Wu, Heavy oil-derived carbon for energy storage application, J. Mater. Chem. A 8 (2020) 7066–7082, doi:10.1039/D0TA00095G.
[32] K.K. Bissada, J.Q. Tan, E. Szymczyk, M. Darnell, M. Mei, Group-type characterization of crude oil and bitumen. Part I: enhanced separation and quantification of saturates, aromatics, resins and asphaltenes (SARA), Org. Geochem. 95 (2016) 21–28, doi:10.1016/j.orggeochem.2016.02.007.
[33] J. Wang, M.A. Gayatri, A.L. Ferguson, Mesoscale simulation and machine learning of asphaltene aggregation phase behavior and molecular assembly landscapes, J. Phys. Chem. B 121 (2017) 4923–4944, doi:10.1021/acs.jpcb.7b02574.
[34] F. Yang, P. Tchoukov, E. Pensini, T. Dabros, J. Czarnecki, J. Masliyah, Z.H. Xu, Asphaltene subfractions responsible for stabilizing water-in-crude oil emulsions. Part 1: interfacial behaviors, Energy Fuels 28 (2014) 6897–6904, doi:10.1021/ef501826g.
[35] F. Yang, P. Tchoukov, H. Dettman, R.B. Teklebrhan, L. Liu, T. Dabros, J. Czarnecki, J. Masliyah, Z.H. Xu, Asphaltene subfractions responsible for stabilizing water-in-crude oil emulsions. Part 2: molecular representations and molecular dynamics simulations, Energy Fuels 29 (2015) 4783–4794, doi:10.1021/acs.energyfuels.5b00657.
[36] J.J. Adams, Asphaltene adsorption, a literature review, Energy Fuels 28 (2014) 2831–2856, doi:10.1021/ef500282p.
[37] J. Neidhardt, Z. Czigány, I. Brunell, L. Hultman, Growth of fullerene-like carbon nitride thin solid films by reactive magnetron sputtering; role of low-energy ion irradiation in determining microstructure and mechanical properties, J. Appl. Phys. 93 (2003) 3002–3015, doi:10.1063/1.1538316.
[38] E. Broitman, W. Zheng, H. Sjöström, I. Ivanov, J. Greene, J. Sundgren, Stress development during deposition of CN x thin films, Appl. Phys. Lett. 72 (1998) 2532–2534, doi:10.1063/1.121410.
[39] Y. Bai, H. Sui, X. Liu, L. He, X. Li, E. Thormann, Effects of the N, O, and S heteroatoms on the adsorption and desorption of asphaltenes on silica surface: a molecular dynamics simulation, Fuel 240 (2019) 252–261, doi:10.1016/j.fuel.2018.11.135.
[40] H.J. Yen, H. Tsai, M. Zhou, E.F. Holby, S. Choudhury, A. Chen, L. Adamska, S. Tretiak, T. Sanchez, S. Iyer, Structurally Defined 3D Nanographene Assemblies via Bottom-Up Chemical Synthesis for Highly Efficient Lithium Storage, Adv. Mater. 28 (2016) 10250–10256, doi:10.1002/adma.201603613.
[41] Y. Xiong, Q. Chen, T.T. Cao, J. Chang, S.M. Xu, Z.H. Xu, Effect of electrolytes on interactions between a novel organic-inorganic hybrid polymer flocculant and kaolinite particles, Colloids Surf., A 590 (2020), doi:10.1016/j.colsurfa.2019.124391.
[42] Q. Chen, S. Xu, Q. Liu, J. Masliyah, Z. Xu, QCM-D study of nanoparticle interactions, Adv. Colloid Interface Sci. 233 (2016) 94–114, doi:10.1016/j.cis.2015.10.004.
[43] A. Natarajan, J.G. Xie, S.Q. Wang, Q.X. Liu, J. Masliyah, H.B. Zeng, Z.H. Xu, Understanding molecular interactions of asphaltenes in organic solvents using a surface force apparatus, J. Phys. Chem. C 115 (2011) 16043–16051, doi:10.1021/jp2039674.
[44] A. Natarajan, N. Kuznicki, D. Harbottle, J. Masliyah, H. Zeng, Z. Xu, Understanding mechanisms of asphaltene adsorption from organic solvent on mica, Langmuir 30 (2014) 9370–9377, doi:10.1021/la500864h.
[45] L. Zhang, C. Zhao, Q. Jian, M. Wu, T. Zhao, A high-performance lithiated silicon-sulfur battery with pomegranate-structured electrodes, J. Power Sources 506 (2021), doi:10.1016/j.jpowsour.2021.230174.
[46] L. Zhang, Q.W. Huang, X.Z. Liao, Y.H. Dou, P.R. Liu, M. Al-Mamun, Y. Wang, S.Q. Zhang, S.L. Zhao, D. Wang, G.W. Meng, H.J. Zhao, Scalable and controllable fabrication of CNTs improved yolk-shelled Si anodes with advanced in operando mechanical quantification, Energy Environ. Sci. 14 (2021) 3502–3509, doi:10.1039/d1ee00639h.
[47] P. Guan, W. Zhang, C. Li, N. Han, X. Wang, Q. Li, G. Song, Z. Peng, J. Li, L. Zhang, X. Zhu, Low-cost urchin-like silicon-based anode with superior conductivity for lithium storage applications, J. Colloid Interface Sci. 575 (2020) 150–157, doi:10.1016/j.jcis.2020.04.082.
[48] G. Zhu, Y. Gu, H. Shuai, Y. Wang, H. Zheng, Simultaneous growth of SiOx/carbon bilayers on Si nanoparticles for improving cycling stability, Electrochim. Acta 323 (2019) 134840, doi:10.1016/j.electacta.2019.134840.
[49] J. Shi, H. Gao, G. Hu, Q. Zhang, Core-shell structured Si@C nanocomposite for high-performance Li-ion batteries with a highly viscous gel as precursor, J. Power Sources 438 (2019) 227001, doi:10.1016/j.jpowsour.2019.227001.
[50] M.X. Tran, J.Y. Woo, T.N. An, S.W. Lee, J.K. Lee, Thermolytically grafted silicon particles with ultrathin carbonaceous coating rich of phenyl moieties as lithium-storage anode material, Chem. Eng. J. 395 (2020) 125169, doi:10.1016/j.cej.2020.125169.
[51] D. Jin, B. Saravanakumar, Y. Ou, G. Li, W. Li, Highly stabilized silicon nanoparticles for lithium storage via hierarchic carbon architecture, ACS Appl. Energy Mater. 3 (2020) 4777–4786, doi:10.1021/acsaem.0c00396.
[52] H.J. Kwon, J.Y. Hwang, H.J. Shin, M.G. Jeong, H.G. Jung, Nano/micro structured silicon-carbon hybrid composite particles fabricated with corn-starch biowaste as anode materials for Li-ion batteries, Nano Lett 20 (2019) 625–635, doi:10.1021/acs.nanolett.9b04395.
[53] H. Wang, J. Fu, C. Wang, J. Wang, A. Yang, C. Li, Q. Sun, Y. Cui, H. Li, A binder-free high silicon content flexible anode for Li-ion batteries, Energy Environ. Sci. 13 (2020) 848–858, doi:10.1039/C9EE02615K.
[54] R. Shao, J. Niu, F. Zhu, M. Dou, Z. Zhang, F. Wang, A facile and versatile strategy towards high-performance Si anodes for Li-ion capacitors: concomitant conductive network construction and dual-interfacial engineering, Nano Energy 63 (2019) 103824, doi:10.1016/j.nanoen.2019.06.020.
[55] Y. An, Y. Tian, H. Wei, B. Xi, S. Xiong, J. Feng, Y. Qian, Porosity-and graphitization-controlled fabrication of nanoporous silicon@ carbon for lithium storage and its conjugation with mxene for lithium-metal anode, Adv. Funct. Mater. 30 (2020) 1908721, doi:10.1002/adfm.201908721.
[56] Y. He, L. Jiang, T.W. Chen, Y.B. Xu, H.P. Jia, R. Yi, D.C. Xue, M. Song, A. Genc, C. Bouchet-Marquis, L. Pullan, T. Tessner, J. Yoo, X.L. Li, J.G. Zhang, S.L. Zhang, C.M. Wang, Progressive growth of the solid-electrolyte interphase towards the Si anode interior causes capacity fading, Nat. Nanotechnol. 16 (2021) 1113, doi:10.1038/s41565-021-00947-8.